



# Variation of the Interplanetary Shocks in the Inner Heliosphere

Rajkumar Hajra

Indian Institute of Technology Indore, Simrol, Indore 453552, India; [raj कुमारhajra@yahoo.co.in](mailto:raj कुमारhajra@yahoo.co.in)

Received 2021 April 9; revised 2021 June 1; accepted 2021 June 1; published 2021 August 23

## Abstract

Observations of the solar wind plasma and interplanetary magnetic field in the ecliptic plane by the Voyager 1 and 2 spacecraft are utilized to study the variation of the interplanetary shocks (with magnetosonic Mach number  $>1$ ) encountered in the inner heliosphere, between  $\sim 1$  and  $\sim 15$  au from the Sun. The overwhelming majority ( $\sim 76\%$ ) of the shocks are fast forward (FF) moving at an average shock speed ( $V_{sh}$ ) of  $\sim 458 \text{ km s}^{-1}$  away from the Sun, and only  $\sim 24\%$  are fast reverse (FR) shocks with an average  $V_{sh}$  of  $\sim 323 \text{ km s}^{-1}$  toward the Sun. About  $\sim 89\%$  of the shocks are quasi-perpendicular with an average shock angle ( $\theta_{Bn}$ ) of  $\sim 72^\circ$  relative to the ambient magnetic field, and only  $\sim 11\%$  are quasi-parallel with an average  $\theta_{Bn}$  of  $\sim 32^\circ$ . While the interplanetary coronal mass ejections are the major ( $\sim 89\%$ ) driver of the FF shocks, a significant part ( $\sim 41\%$ ) of the FR shocks are associated with the corotating interaction regions. The shock occurrence rate, with a peak at the heliocentric distance ( $R_h$ ) of  $\sim 5$  au, exhibits a clear decrease with the increasing  $R_h$ . While the shock strength and propagation angle do not exhibit any systematic change with  $R_h$ ,  $V_{sh}$  increases with the increasing  $R_h$  at a rate of  $\sim 11 \text{ km s}^{-1} \text{ au}^{-1}$ .

*Unified Astronomy Thesaurus concepts:* [Interplanetary shocks \(829\)](#); [Solar coronal mass ejections \(310\)](#); [Corotating streams \(314\)](#); [Interplanetary magnetic fields \(824\)](#); [Solar wind \(1534\)](#)

## 1. Introduction

Interplanetary shocks are discontinuous spatial changes in the solar wind plasma and interplanetary magnetic field (IMF), involving both mass flow and magnetic field penetration across their surfaces (Landau & Lifshitz 1960; Kennel et al. 1985; Tsurutani et al. 2011). Fast interplanetary shocks are formed by the nonlinear steepening of the fast-mode magnetohydrodynamic (MHD) waves, and they propagate through the interplanetary medium at speeds greater than the ambient upstream magnetosonic wave speed ( $V_{ms}$ ). These can be fast forward (FF) or fast reverse (FR) shocks depending on their propagation in the same or opposite directions of their drivers, respectively. However, as the propagation speeds are less than the ambient solar wind speed, both the FF and FR shocks are convected by the solar wind flow.

While interplanetary shocks are thin/small-scale transient disturbances, these are driven by the large-scale transient disturbances like coronal mass ejections (CMEs), solar wind high-speed streams (HSSs) or corotating interaction regions (CIRs), which propagate from the Sun to the interplanetary medium. Fast interplanetary CMEs (ICMEs) propagating (with speed from  $\sim 500$  to  $>2000 \text{ km s}^{-1}$ ) faster than the local upstream  $V_{ms}$  (typically  $\sim 70$ – $100 \text{ km s}^{-1}$ ) in the plasma frame, can generate upstream FF shocks followed by sheaths of compressed, heated, and turbulent solar wind plasma and large-amplitude IMF variations (e.g., Kennel et al. 1985; Tsurutani et al. 1988). Thus, the plasma temperature, density, and IMF intensity increase in the sheath downstream of the FF shocks. In contrast, these parameters decrease in the sheath following the FR shocks owing to sunward propagation of the FR shocks for which the sunward side is in the upstream unshocked region. On the other hand, coronal hole emanated HSSs (with speed of  $\sim 500$ – $850 \text{ km s}^{-1}$ ) can compress the ambient slow ( $\sim 300$ – $400 \text{ km s}^{-1}$ ) solar wind. The compressed plasma region corotates with the Sun, and is called a CIR (Siscoe 1972; Smith & Wolfe 1976; Balogh et al. 1999). At large heliocentric distances ( $R_h$ ), where the relative speed between a HSS and the background solar wind is higher than the

characteristic speed of the local medium, the CIR is bounded by a pair of FF and FR shocks at the leading and trailing edges, respectively (Sonett & Colburn 1965; Smith & Wolfe 1976; Burlaga et al. 1990; Tsurutani et al. 1995; Echer et al. 2010; Hajra et al. 2018).

Thus, the interplanetary shocks can be useful for monitoring the large-scale space weather events (e.g., ICMEs, CIRs, and HSSs) and their evolution in the heliosphere. This is the main aim of the present work. Several works have reported the evolution of the shocks with  $R_h$  due to evolution of the solar wind (see Behannon 1978; Balogh et al. 1993; Hoang et al. 1995; Luhmann 1995; Gazis 1996; González-Esparza et al. 1998; Burlaga et al. 2002; Richardson & Wang 2005; Neugebauer 2013; Richardson 2014; Echer 2019a, 2019b, and references therein). While the majority of the shocks at  $\sim 1$  au are shown to be driven by ICMEs (Cane 1985; Sheeley et al. 1985; Kilpua et al. 2015), CIRs are fully developed with the FF–FR shock pair at  $>1.5$ – $2$  au and drive a significant part of the shocks at  $\geq 3$  au (Hundhausen & Gosling 1976; Smith & Wolfe 1976; Hajra et al. 2018). The cited works greatly contributed to our understanding of the shock evolution in the interplanetary space. However, there is no detailed study on the shock characteristic parameters and their variation in the inner heliosphere. In particular, we would like to refer to the work by Richardson & Wang (2005) that surveyed all the solar wind/interplanetary discontinuities observed by Voyager 2 out to 75 au. However, the solar wind plasma discontinuities were simply identified as shocks, and no proper shock analysis was performed. It should be noted that the plasma discontinuities could be shocks or waves depending on the magnetosonic Mach number ( $M_{ms}$ ) greater or less than unity, which was not verified. The shock normal, angle of propagation, and Mach number are important characteristic parameters to understand the dynamics and morphology, which were not explored in Richardson & Wang (2005). In addition, they did not identify the interplanetary drivers of the individual shocks, and how their relative importance vary with  $R_h$ . In other words, there is ample scope for a deeper exploration of the shocks encountered by Voyager. In the present work, we will utilize the solar wind plasma and IMF

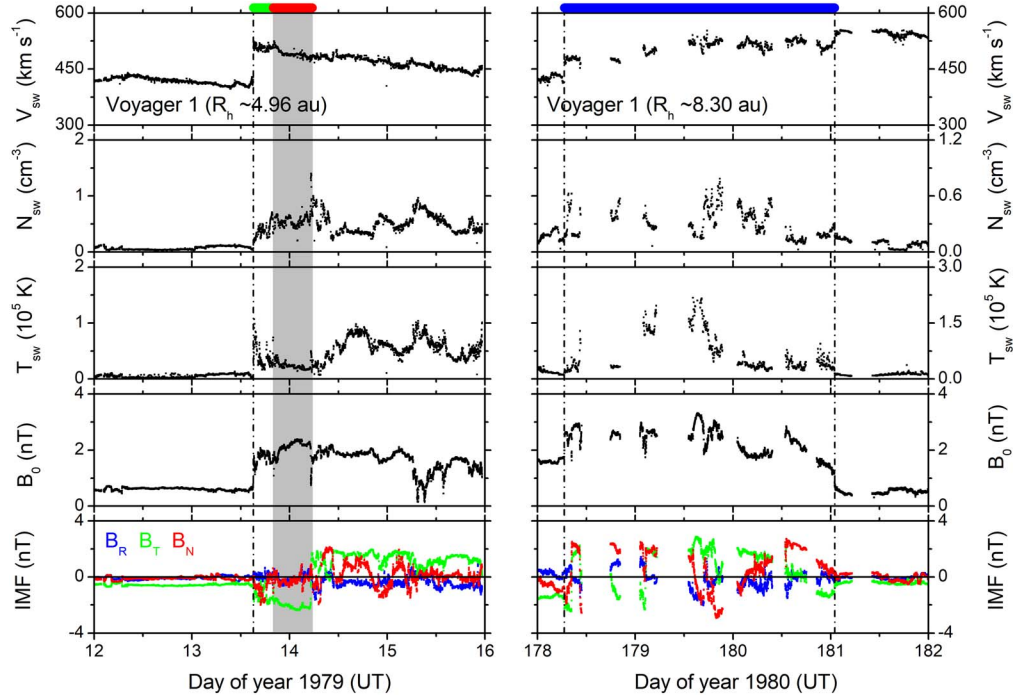


**Figure 1.** Examples of the interplanetary shocks and their drivers. From top to bottom, the panels show the solar wind plasma speed ( $V_{sw}$ ), density ( $N_{sw}$ ), temperature ( $T_{sw}$ ), IMF magnitude ( $B_0$ ), and components  $B_R$ ,  $B_T$ , and  $B_N$ , respectively. The left and right panels show the Voyager 1 observations during 1979 January 12–15, and 1980 June 26–29, respectively. Interplanetary shocks are shown by the vertical dashed–dotted lines. Horizontal bars at the top panel show the interplanetary sheath (green), MC (red), and CIR (blue). MC is also marked by a gray shading.

measurements by the twin spacecraft Voyager 1 and 2 from  $R_h \sim 1$  to  $\sim 15$  au (beyond which the shock detection in the ecliptic plane decreased significantly) to identify all the shocks encountered by them in the ecliptic plane of the Sun, to classify the shocks, to identify their interplanetary drivers, and to characterize the shocks in terms of their speed, propagation angle, Mach number, and plasma density and magnetic field compression strength. Variation of the shocks and their characteristic parameters with  $R_h$  will be explored in detail. This study will hopefully augment our understanding of the space weather events and their evolution.

## 2. Data Analysis and Results

### 2.1. Detection of Interplanetary Shocks and Their Drivers: Examples

Figure 1 shows examples of the interplanetary shocks and associated interplanetary drivers as detected by the Voyager 1 spacecraft. From top to bottom, the panels are the solar wind plasma speed ( $V_{sw}$ ), density ( $N_{sw}$ ), temperature ( $T_{sw}$ ), IMF magnitude ( $B_0$ ), and IMF components  $B_R$ ,  $B_T$ , and  $B_N$ , respectively. The IMF data are in the spacecraft-centered radial tangential normal (RTN) coordinate system, where  $\hat{R}$  is the unit vector directed from the Sun to the spacecraft, and  $\hat{T} = \Omega \times \hat{R} / |\Omega \times \hat{R}|$ , where  $\Omega$  is the Sun’s spin axis. The right-hand system is completed by  $\hat{N}$ . The high-resolution data are obtained from NASA’s COHWeb (<https://omniweb.gsfc.nasa.gov/coho/>), which provides access to the heliospheric magnetic field, plasma, and spacecraft position data for several spacecraft.

During 1979 January 12–15 (days 12 through 15 of the year), when Voyager 1 was at  $R_h \sim 4.96$  au, it encountered an

ICME (Figure 1, left panels). The fast ( $V_{sw} \sim 524 \text{ km s}^{-1}$ ) ICME, propagating faster than the upstream plasma by more than the local magnetosonic speed ( $V_{ms} \sim 61 \text{ km s}^{-1}$ ), generated an interplanetary shock at  $\sim 15:07$  UT on day 13 (shown by the vertical dashed–dotted line), identified by sudden increases in the solar wind plasma parameters.  $V_{ms}$  is estimated as  $\sqrt{V_A^2 + V_s^2}$ , where  $V_A$  is the Alfvén speed ( $B_0 / \sqrt{\mu_0 \rho}$ ), and  $V_s$  is the sound speed ( $\sqrt{5k_B(T_p + T_e)/3m_p}$ ),  $\mu_0$  is the free space permeability,  $\rho$  denotes the solar wind mass density,  $k_B$  is the Boltzmann constant,  $T_p$  and  $T_e$  are the proton and electron temperatures, respectively, and  $m_p$  is the proton mass. Considering the upstream and downstream intervals of  $\sim 10$  minutes around the shock, the shock is characterized by sharp increases in  $V_{sw}$  from  $\sim 399$  to  $\sim 524 \text{ km s}^{-1}$ , in  $N_{sw}$  from  $\sim 0.1$  to  $\sim 0.3 \text{ cm}^{-3}$ , in  $T_{sw}$  from  $\sim 0.1 \times 10^5$  to  $\sim 1.1 \times 10^5 \text{ K}$ , and in  $B_0$  from  $\sim 0.6$  to  $\sim 1.8 \text{ nT}$ . The magnetic field ratio ( $r_B \sim 3.0$ ) and plasma density ratio ( $r_N \sim 3.0$ ) between the downstream and upstream solar wind are defined as the shock compression. Due to the simultaneous increases in  $V_{sw}$ ,  $N_{sw}$ ,  $T_{sw}$ , and  $B_0$  across the shock, it is classified as a FF shock.

The upstream and downstream plasma (speed) and IMF vectors are utilized to determine the shock normal  $\hat{n}$  using the mixed-mode technique (Abraham-Shrauner & Yun 1976):

$$\hat{n} = \frac{(\Delta \mathbf{B} \times \Delta \mathbf{V}_{sw}) \times \Delta \mathbf{B}}{|(\Delta \mathbf{B} \times \Delta \mathbf{V}_{sw}) \times \Delta \mathbf{B}|}, \quad (1)$$

where  $\Delta \mathbf{B} (= \mathbf{B}_d - \mathbf{B}_u)$  and  $\Delta \mathbf{V}_{sw} (= \mathbf{V}_d - \mathbf{V}_u)$  are the IMF and  $V_{sw}$  jumps, respectively, subscripts  $u$  and  $d$  denote the upstream and downstream values across the shocks. The shock normal is found to be  $[0.92, 0.29, -0.26]$ .

Assuming the conservation of mass flux in the shock rest frame, the shock speed  $V_{\text{sh}}$  is estimated as

$$V_{\text{sh}} = \frac{\hat{n} \cdot (\rho_d \mathbf{V}_d - \rho_u \mathbf{V}_u)}{\rho_d - \rho_u}. \quad (2)$$

$V_{\text{sh}}$  along the shock normal is determined to be  $\sim 531 \text{ km s}^{-1}$ . The shock angle ( $\theta_{\text{Bn}}$ ) between the shock normal  $\hat{n}$  and the upstream IMF vector is determined to be  $\sim 82.8^\circ$ , implying this to be a quasi-perpendicular shock. The magnetosonic Mach number  $M_{\text{ms}}$ , defined as the ratio of  $V_{\text{sh}}$  (relative to the upstream  $V_{\text{sw}}$ ) to the upstream  $V_{\text{ms}}$ , is computed to be  $\sim 2.2$  (confirming it to be a shock, not a wave). Thus, the FF shock at  $\sim 15:07$  UT on day 13 detected at  $\sim 4.96$  au is found to be a quasi-perpendicular shock propagating at a relative speed  $\sim 2.2$  times of the ambient magnetosonic speed at an angle of  $\sim 82.8^\circ$  relative to the ambient magnetic field. Detail description of the shock analysis method by solving the Rankine–Hugoniot conservation equations (Rankine 1870; Hugoniot 1887, 1889) can be found in literature (e.g., Smith 1985; Tsurutani & Lin 1985; Tsurutani et al. 2011; Hajra et al. 2016, 2020; Hajra & Tsurutani 2018a).

The FF shock on day 13 is followed by a downstream interplanetary sheath from  $\sim 15:07$  to  $\sim 20:00$  UT on day 13 (shown by a green bar on the top, Figure 1, left panel). Following the sheath, the shaded region (marked by a red bar on the top, Figure 1, left panel), from  $\sim 20:00$  UT on day 13 to  $\sim 05:36$  UT on day 14, is characterized by an enhanced IMF  $B_0$ , smooth and slow rotation in  $B_T$ , and reduced  $T_{\text{sw}}$ . These are the typical signatures of a flux rope magnetic cloud (MC; Burlaga et al. 1981; Klein & Burlaga 1982; Tsurutani & Gonzalez 1997) in the interplanetary space.

A CIR was encountered by Voyager 1 when it was at  $R_h \sim 8.30$  au during 1980 June 26–29 (between days 178 and 181 of the year). The CIR (marked by a blue bar on the top, Figure 1, right panel) can be identified between a slow-speed stream with  $V_{\text{sw}} \sim 419 \text{ km s}^{-1}$  on day 178 and a coronal hole emanated HSS with  $V_{\text{sw}} \sim 552 \text{ km s}^{-1}$  on day 181. The CIR is a compressed plasma characterized by high plasma density ( $N_{\text{sw}} \sim 0.7 \text{ cm}^{-3}$ ), temperature ( $T_{\text{sw}} \sim 2.2 \times 10^5 \text{ K}$ ), and magnetic field ( $B_0 \sim 3.0 \text{ nT}$ ) compared to the ambient plasma. Most interestingly, the CIR is bounded by two shocks at its leading and trailing ends.

At  $\sim 06:33$  UT on day 178 (at the CIR leading edge), a sharp increase in  $V_{\text{sw}}$  from  $\sim 427$  to  $\sim 484 \text{ km s}^{-1}$  is accompanied by increases in  $N_{\text{sw}}$  from  $\sim 0.2$  to  $\sim 0.3 \text{ cm}^{-3}$ , in  $T_{\text{sw}}$  from  $\sim 0.1 \times 10^5$  to  $\sim 0.2 \times 10^5 \text{ K}$ , and in  $B_0$  from  $\sim 1.7$  to  $\sim 2.5 \text{ nT}$ . By definition, this is an FF shock with the compression ratios of  $r_B \sim 1.5$  and  $r_N \sim 1.5$ . Following the above-mentioned techniques, the FF is found to be propagating with a speed  $V_{\text{sh}} \sim 557 \text{ km s}^{-1}$  at an angle  $\theta_{\text{Bn}} \sim 87.2^\circ$  relative to the ambient IMF. The estimated  $M_{\text{ms}}$  is  $\sim 1.3$ . The result implies that the FF shock detected at  $\sim 8.30$  au was quasi-perpendicular, propagating at a relative speed of  $\sim 1.3$  times the magnetosonic speed at an angle  $\sim 87.2^\circ$  relative to the ambient magnetic field.

The shock at the trailing edge of the CIR, at  $\sim 00:59$  UT on day 181, is characterized by a sharp increase in  $V_{\text{sw}}$  from  $\sim 507$  to  $\sim 532 \text{ km s}^{-1}$ , accompanied by simultaneous sharp decreases in  $N_{\text{sw}}$  from  $\sim 0.3$  to  $\sim 0.2 \text{ cm}^{-3}$ , in  $T_{\text{sw}}$  from  $\sim 0.3 \times 10^5$  to  $\sim 0.1 \times 10^5 \text{ K}$ , and in  $B_0$  from  $\sim 1.1$  to  $\sim 0.6 \text{ nT}$ . This is defined as an FR shock. The FR shock propagates toward the Sun, but because the solar wind carrying the shock has a higher speed,

the FR shock is also convected in the anti-sunward direction. The FR has the compression ratios of  $r_B \sim 1.8$  and  $r_N \sim 1.5$ . The FR shock is estimated to be propagating with a speed  $V_{\text{sh}} \sim 476 \text{ km s}^{-1}$  at an angle  $\theta_{\text{Bn}} \sim 58.3^\circ$  relative to the ambient IMF. The estimated  $M_{\text{ms}}$  is  $\sim 1.3$ . Thus, the FR shock at the CIR trailing edge, detected at  $\sim 8.30$  au, was a quasi-perpendicular shock propagating at a speed  $\sim 1.3$  times of the local magnetosonic speed at a comparatively smaller angle of  $\sim 58.3^\circ$  relative to the ambient magnetic field.

## 2.2. Heliocentric Variation of the Shock Parameters

Using the method discussed above (Section 2.1), all the interplanetary shocks encountered by the Voyager 1 and 2 spacecraft in the ecliptic plane (in the heliolatitude range of  $\pm 10^\circ$ ) were identified. The method can be summarized as follows. First, from the temporal variations of the solar wind plasma and IMF, the abrupt increases in  $V_{\text{sw}}$  with simultaneous increases/decreases in  $N_{\text{sw}}$ ,  $T_{\text{sw}}$ , and  $B_0$  were identified as potential shocks. Second, values of the solar wind plasma and IMF across the potential shocks were used to estimate  $V_A$ ,  $V_S$ ,  $V_{\text{ms}}$ , and  $M_{\text{ms}}$  as defined in Section 2.1. The discontinuities with only  $M_{\text{ms}} > 1$  were confirmed as shocks. Voyager 1 encountered 44 shocks from 1977 September to 1980 June in the  $R_h$  range of  $\sim 1$ – $8.3$  au. Voyager 2 identified 76 shocks from 1977 September to 1984 October between  $R_h$  of  $\sim 1$  and  $\sim 15.2$  au. Beyond these periods, Voyager 1 did not encounter any shock, Voyager 2 encountered only two shocks, at  $\sim 29$  au on 1989 February 25 and at  $\sim 32$  au on 1990 March 16, with  $M_{\text{ms}}$  of  $\sim 4.5$  and  $\sim 4.8$ , respectively. Thus, these were not included in the statistical analysis. While the spacecraft data coverage did not change much beyond  $\sim 15$  au, several causes, like movement of the spacecraft to the off-ecliptic plane, data quality, change in the solar wind character etc., might be responsible for the drastic decrease in the shock detection in the ecliptic plane beyond  $\sim 15$  au. It may be mentioned that with much *relaxed* criteria, Richardson & Wang (2005) identified quite a significant number of discontinuities (encountered by Voyager 2) beyond  $\sim 15$  au; however, they also confirm a large decrease in the number.

The heliocentric and solar cycle dependencies of the 120 shocks (with  $M_{\text{ms}} > 1$ ) identified between  $\sim 1$  and  $\sim 15$  au are explored in Figure 2. According to the monthly mean smoothed sunspot numbers, the solar cycle 21 started during 1976 March, attained the maximum during 1979 December, and ended during 1986 September. Thus, the period under study (1977 September through 1984 October) covers the ascending, maximum, and descending phases of the solar cycle. This is also reflected in the  $F_{10.7}$  solar flux variation (Figure 2(a)).

The shock occurrence ( $N_{\text{sh}}$ ) shows a clear peak around 5 au, after which the occurrence decreases with the increasing  $R_h$  (Figure 2(b), (c)). However, owing to varying speed of the spacecraft at different  $R_h$ , the observation period (or the spacecraft time spent TS in each  $R_h$  bin) varied largely at different locations (Figure 2(b), (c), red horizontal steps, legend on the right). To account for this varying observation period,  $N_{\text{sh}}$  at each  $R_h$  bin was normalized by the observation period at that bin ( $N_{\text{sh}} \text{ TS}^{-1}$ ). The result is shown in Figure 2(d). This shows the peak occurrence at  $\sim 1$  au, a second and comparable peak around 5 au, followed by a sharp fall in the shock occurrence rate. However, on the average, normalized  $N_{\text{sh}}$  exhibits a linear decrease with the increasing  $R_h$  (Table 1). Normalized  $N_{\text{sh}}$  and  $R_h$  are strongly



**Table 1**  
Relationships of the Shock Parameters with  $R_h$

Parameter	Relationship with $R_h$	Correlation Coefficient ( $r$ )	Significance Level
Normalized $N_{sh}$	$N_{sh} TS^{-1} = 1.72 - 0.11R_h$	-0.86	>99%
$V_{sh}$	$V_{sh} = 380.71 + 10.57R_h$	0.67	>99%
$M_{ms}$	$M_{ms} = 1.39 + 0.10R_h$	0.58	>95%
$r_N$	$r_N = 2.14 - 0.03R_h$	-0.47	>90%

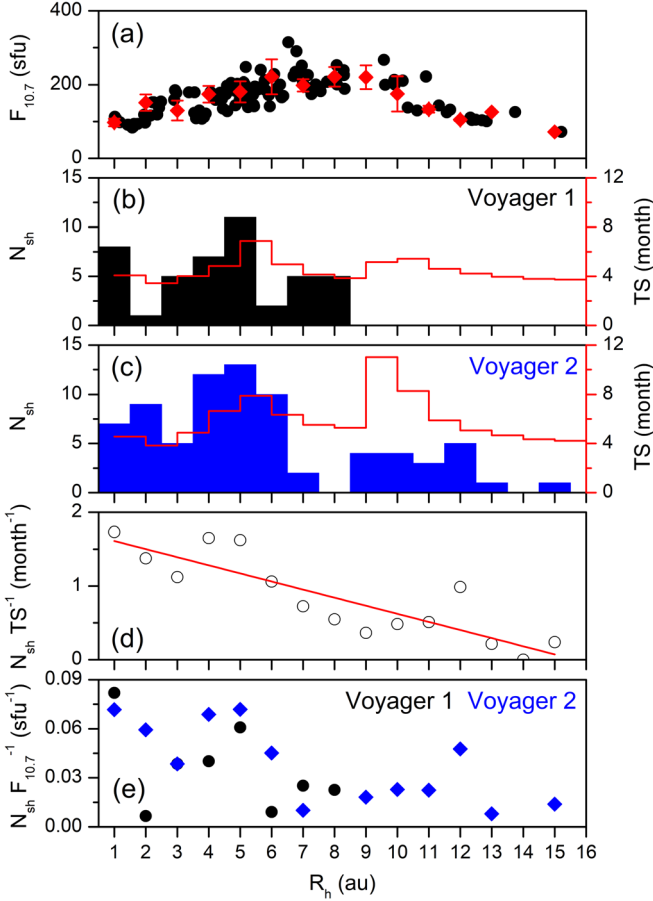


**Figure 2.** Variation of the interplanetary shocks with the heliocentric distance ( $R_h$ ). (a) The  $F_{10.7}$  solar flux daily values (black circles), means (red diamonds) and standard deviations (vertical bars), (b) number of the shocks ( $N_{sh}$ ) observed by Voyager 1 (black histograms, legend on the left) and time spent (TS) by the spacecraft in each  $R_h$  bin (red horizontal steps, legend on the right), (c)  $N_{sh}$  observed by Voyager 2 (blue histograms, legend on the left) and TS by the spacecraft in each  $R_h$  bin (red horizontal steps, legend on the right), (d)  $N_{sh}$  normalized by TS (empty circles) along with linear regression line (red line), and (e)  $N_{sh}$  normalized by  $F_{10.7}$ . In panel (e), black circles and blue diamonds correspond to the observations made by Voyager 1 and 2, respectively.  $F_{10.7}$  is expressed in the solar flux unit (sfu), where the sfu is  $10^{-22} \text{ W m}^{-2} \text{ Hz}^{-1}$ .

anticorrelated (correlation coefficient  $r = -0.86$ ) at a confidence level of >99% (Student's t-test; Student 1908).

As the solar activity ( $F_{10.7}$ ) largely varied during the study interval, the shock occurrence was also normalized by the  $F_{10.7}$  solar flux (Figure 2(e)) to separate the solar activity contribution from the radial variation of the shocks. The solar flux normalized  $N_{sh}$  ( $N_{sh} F_{10.7}^{-1}$ ) also exhibits a similar shock occurrence pattern as above: the peak occurrences at  $\sim 1$  and  $\sim 5$  au, followed by a sharp fall in the shock occurrence at the larger  $R_h$ .

The occurrence peak of the shocks at  $\sim 5$  au from the Sun, and decrease at the larger distances are consistent with previous results (e.g., Hoang et al. 1995; Luhmann 1995; González-Esparza et al. 1996, 1998; Richardson & Wang 2005; Neugebauer 2013; Echer 2019a, 2019b, and references therein). However, most of the previous reports are obtained from compilation of different spacecraft observations at different heliocentric distances, and during varying solar activity condition. However, the present work separates the solar activity contribution from the radial variation of the shocks.

The shocks identified above are classified into two groups: (1) the FF shocks characterized by the sharp increases in  $V_{sw}$ ,  $N_{sw}$ ,  $T_{sw}$ , and IMF  $B_0$ , and (2) the FR shocks characterized by a sharp increase in  $V_{sw}$  with simultaneous decreases in  $N_{sw}$ ,  $T_{sw}$ , and  $B_0$ . The interplanetary drivers are identified for each of the shocks as ICME or CIR following the method described in Section 2.1. From the temporal variations of the solar wind plasma and IMF, a CIR is identified as the region of the compressed (high) plasma density  $N_{sw}$  and IMF magnitude  $B_0$  between a slow stream and an HSS (Smith & Wolfe 1976). The shock driver is classified as an ICME when the shock is followed by a sheath characterized by the downstream high  $T_{sw}$ ,  $N_{sw}$  and  $B_0$  (Kennel et al. 1985; Tsurutani et al. 1988). This is sometimes followed by an MC characterized by a high  $B_0$ , a smooth and slow rotation in the IMF component(s), and a reduced  $T_{sw}$  (Burlaga et al. 1981). The shock characteristic parameters  $V_{sh}$ ,  $\theta_{Bn}$ ,  $M_{ms}$ ,  $r_B$ , and  $r_N$ , as shown in Section 2.1, are determined for each of the shocks. Figure 3 shows the variations of the shock types (FF and FR, Figure 3(a)), their interplanetary drivers (ICME and CIR, Figure 3(b), (c)), shock parameters  $V_{sh}$  (Figure 3(d)),  $\theta_{Bn}$  (Figure 3(e)),  $M_{ms}$  (Figure 3(f)),  $r_B$  (Figure 3(g)), and  $r_N$  (Figure 3(h)), and the  $F_{10.7}$  solar flux (Figure 3(i)) with  $R_h$ .

Among all 120 shocks,  $\sim 76\%$  are FF and only  $\sim 24\%$  are FR type. The relative occurrence of the FF and FR shocks at different  $R_h$  is shown in Figure 3(a). While a larger percent of the shocks are of the FF type at any  $R_h$ , the FR percent increases gradually from  $\sim 1$  au and attains a peak around 7–8 au, after which it decreases again. The relative occurrence of the FF and FR shocks, and their heliocentric variation shown in Figure 3(a) are also consistent with previous reports. For example, at  $\sim 1$  au,  $\sim 66\%$ – $88\%$  of the shocks are reported to be FF depending on the solar cycle phase (Echer et al. 2003; Kilpua et al. 2015). At  $\sim 5$  and  $\sim 10$  au, the FF shocks are  $\sim 69\%$ – $72\%$  (Echer et al. 2010; Echer 2019a) and  $\sim 75\%$  (Echer 2019b) of all shocks, respectively.

The relative role of the interplanetary drivers (ICMEs and CIRs) is shown in Figures 3(b) and (c). As the ICMEs and CIRs exhibit the distinguished solar cycle variations (Sheeley et al. 1976; Burlaga et al. 1981; Gosling et al. 1990; Tsurutani et al. 1995, 2020; Gopalswamy et al. 2004; Obridko et al. 2012; Hajra et al. 2013, 2014; Hajra & Tsurutani 2018b; Hajra 2021), results in Figures 3(b) and (c) should be discussed with reference to the solar activity ( $F_{10.7}$ , Figure 3(i)) variation. The solar maximum (and a few years around the maximum) is dominated by sunspots, active regions, solar flares, CMEs, or ICMEs. The occurrence rate

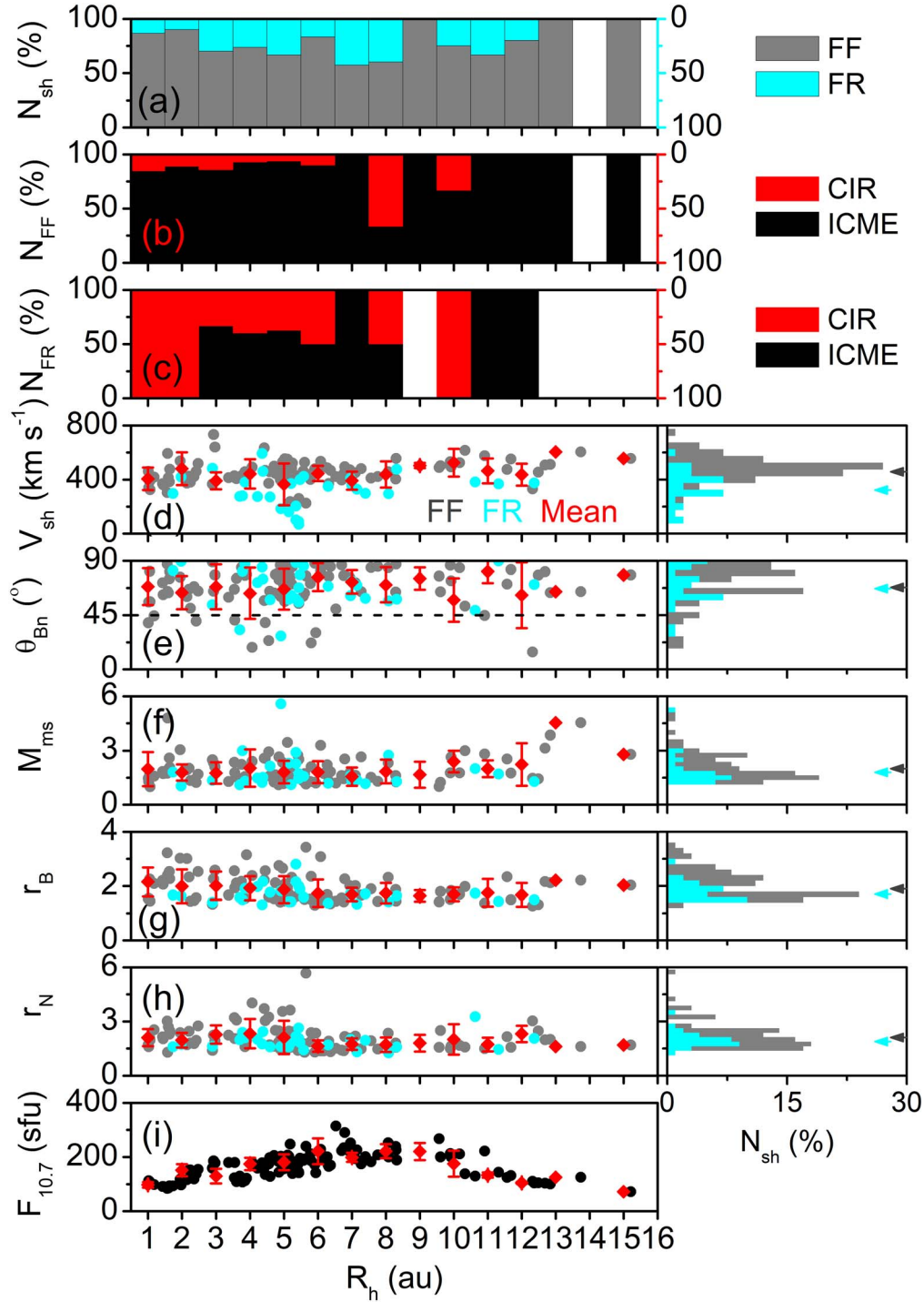


**Figure 3.** Variations of the interplanetary shocks and shock parameters with ( $R_h$ ). (a) Distribution of the FF (gray) and FR (cyan) shocks, (b) distribution of the FF shocks caused by ICMEs (black) and CIRs (red), (c) distribution of the FR shocks caused by ICMEs (black) and CIRs (red), variations of (d) the shock speed  $V_{sh}$ , (e) shock angle  $\theta_{Bn}$ , (f) magnetosonic Mach number  $M_{ms}$ , (g) compression ratio of the magnetic field  $r_B$ , (h) compression ratio of the plasma density  $r_N$  across the shocks, (i)  $F_{10.7}$  solar flux. In panels (d)–(h), the gray and cyan circles represent the values for the FF and FR shocks, respectively, while the red diamonds with vertical bars show the mean and standard deviations for all shocks. Histograms on the right (panels (d)–(h)) show the distribution of the shocks for different ranges of the parameters. The mean values are indicated by horizontal arrows. The panel (i) is in the same format as Figure 2(a).

of ICMEs decreases with the decreasing  $F_{10.7}$ . On the contrary, the interplanetary space (in the ecliptic plane) is dominated by HSSs and CIRs during the descending and solar minimum phases when coronal holes extend to the lower solar latitudes and expand in size. For the entire period of observation (irrespective of the solar activity variation), ICMEs are found to be the major driver of the FF shocks, driving  $\sim 89\%$  of the FF shocks, while only  $\sim 11\%$

of the FF shocks are driven by CIRs. However,  $\sim 59\%$  of the FR shocks are associated with ICMEs and  $\sim 41\%$  with CIRs. Thus, CIRs are a significant driver for the FR shocks. Interestingly, around 1–2 and 10 au, all FR shocks are driven by CIRs (Figure 3(d)). As can be found from the  $F_{10.7}$  variation (Figure 3(i)), these locations were traveled by the spacecraft during the solar minimum-to-ascending and the descending

phases, respectively. In addition, around 8 au (after the solar maximum), CIRs are found to be the dominating driver of the FF ( $\sim 67\%$ ) and FR ( $\sim 50\%$ ) shocks, compared to ICMEs.

The above results clearly contradict the results of Echer (2019a), reporting  $\sim 90\%$  of the FR shocks being driven by CIRs, and more or less equal distribution of the FF shocks between ICMEs ( $\sim 55\%$ ) and CIRs ( $\sim 45\%$ ) at  $\sim 5$  au. While the FR shock formation in association with ICMEs is quite rare, they may result from the speed differences between the fast solar wind following slower stream (Gosling et al. 1988), or owing to an overexpansion of an ICME (Gosling et al. 1994). In addition, the present results are interesting, also because it was previously reported that only few CIRs are bounded by shocks at  $\sim 1$  au (e.g., Tsurutani et al. 1995; Jian et al. 2006). As shock formation through the nonlinear steepening of the large-amplitude magnetosonic waves theoretically requires several nonlinear steepening times, shocks typically form at the leading and trailing edges of CIRs only at the large  $R_h$  ( $> 1.5$ – $2.5$  au).

In the entire  $R_h$  range of the study, the shock speed  $V_{sh}$  exhibits a large variation (Figure 3(d), right panel): from  $\sim 226$  to  $\sim 733$  km s $^{-1}$  with an average  $V_{sh}$  of  $\sim 458$  km s $^{-1}$  for the FF shocks, and from  $\sim 68$  to  $\sim 593$  km s $^{-1}$  with an average  $V_{sh}$  of  $\sim 323$  km s $^{-1}$  for the FR shocks. The statistical significance of this result is assessed by the Student's  $t$ -statistics and estimation of the corresponding probability factor  $p$  (Reiff 1990; Press et al. 1992). A  $p$  value of  $< 0.0001$  was estimated, implying that the higher speed of the FF shocks compared to the FR shocks is statistically significant. At any  $R_h$ , the FF shocks seem to have higher speed than the FR shocks. On the average,  $V_{sh}$  exhibits a slow increase at a rate of  $\sim 10.57$  km s $^{-1}$  au $^{-1}$  with the increasing  $R_h$  (Table 1).  $V_{sh}$  is correlated (correlation coefficient  $r = 0.67$ ) to  $R_h$  at a high significance level ( $> 99\%$ ).

The shock propagation angle  $\theta_{Bn}$  does not exhibit any clear dependence on  $R_h$  (Figure 3(e), left panel). The overwhelming majority,  $\sim 88\%$  of the FF shocks and  $\sim 93\%$  of the FR shocks, are found to be quasi-perpendicular (with  $\theta_{Bn} > 45^\circ$ ), and only  $\sim 12\%$  of the FF and  $\sim 7\%$  of the FR shocks are quasi-parallel ( $\theta_{Bn} \leq 45^\circ$ ) (Figure 3(e), right panel). It is interesting to note that after  $\sim 6$  au, only two shocks are observed to be quasi-parallel. These results are consistent with previous results reporting dominance of the quasi-perpendicular shocks at  $R_h$  of  $\sim 1$  au (Bavassano-Cattaneo et al. 1986; Neugebauer 2013; Kilpua et al. 2015),  $\sim 5$  au (Echer 2019a), and  $\sim 10$  au (Echer 2019b). It can be noted that IMF, from an average orientation angle of  $\sim 45^\circ$  to the ecliptic plane at  $\sim 1$  au, becomes more and more tangential at the larger  $R_h$  (e.g., Parker 1965; Behannon 1978). This makes the shocks more likely to be quasi-perpendicular.

The heliocentric variations of the shock strength parameters ( $M_{ms}$ ,  $r_B$ , and  $r_N$ ) are shown in Figures 3(f)–(h). No clear distinction can be made between the FF and FR shocks. From the linear regression analysis,  $M_{ms}$  is found to increase slowly with the increasing  $R_h$  at a rate of  $\sim 0.10$  au $^{-1}$ , while  $r_N$  decreases with the increasing  $R_h$  at a rate of  $\sim -0.03$  au $^{-1}$  (Table 1). However, the corresponding correlation ( $r = 0.58$ ) and anticorrelation ( $r = -0.47$ ) coefficients, respectively, of the linear regression analysis are not high. It is interesting to note that Echer (2019a) compared the shock compression ratio and  $M_{ms}$  at  $\sim 1$ ,  $\sim 5$ , and  $\sim 10$  au based on data from several independent works, and concluded that the shock strength increases from  $\sim 1$  to  $\sim 5$  au, and then decreases from  $\sim 5$  to  $\sim 10$  au. However, the present work, with a much continuous and larger database, reveals no prominent systematic shock

strength variation with  $R_h$ . This was also concluded by Richardson & Wang (2005) using the upstream to downstream density ratios across the interplanetary discontinuities.

### 3. Discussion and Conclusions

A detailed study on the radial distributions of shock occurrences in the ecliptic plane, shock characteristics, and their drivers in the inner heliosphere is presented. It reveals a complex dynamics related to the space weather events and their interplanetary evolution.

About 65% of all shocks identified between  $\sim 1$  and  $\sim 15$  au from the Sun were encountered at  $\lesssim 5$  au, beyond which the shock occurrence decreases very fast. When normalized by the spacecraft observation time in different heliocentric locations, the shock occurrence rate clearly exhibits a peak around 5 au, and an overall decrease with the increasing  $R_h$ . As shocks detected only in the ecliptic plane ( $\pm 10^\circ$  heliolatitudes) are considered in this work, this result largely depends on the morphology, orientation, and evolution of the shock drivers and their evolution with respect to the ecliptic plane and  $R_h$ . Another important factor is the change in the character of the solar wind beyond the hydrogen ionization cavity (Holzer 1972; Zank 1999) which is located within  $\sim 5$ – $8$  au. Beyond this region, the solar wind is mediated by the interstellar pickup ions ( $H^+$ ,  $He^+$ ) that dominate the internal energy of the solar wind (e.g., Zank et al. 2018). As a result, temperature of the pickup ion mediated solar wind increases with  $R_h$  leading to a significant increase in the sound speed outside the cavity. This plays an important role in modulating the dynamics and morphology of the interplanetary shocks (e.g., Zank & Pauls 1997; Rice & Zank 1999; Rice et al. 2000), such as increase in the shock propagation speed, decay in the compression ratio, and formation of multiple forward–reverse shock pairs with the increasing  $R_h$ .

While only a few FF shocks are associated with CIRs, all of the FR shocks around 1–2 and 10 au are driven by CIRs. At other locations as well, CIRs are found to be a significant source of the FR shocks. This result may indicate that in the ecliptic plane probability of the FR shock formation at the trailing edge of a CIR is larger than that of the FF shock formation at a CIR leading edge in the inner heliosphere. This can be verified by a further study on the CIR evolution in the ecliptic plane.

On the average, the FF shock speed is significantly higher than the FR shock speed. However, no clear distinction can be made in the shock propagation angle, and the shock strength between the FF and FR shocks. In addition, the shock strength and propagation angle essentially do not exhibit any systematic change with  $R_h$ . However, the average shock speed is found to increase slowly at a rate of  $\sim 11$  km s $^{-1}$  au $^{-1}$ . Wang et al. (2001), using the MHD numerical modeling, predicted a decrease in the radial solar wind velocity with  $R_h$ . The decrease in the background solar wind speed is conducive and consistent with an increase in the shock speed. This result is also consistent with the increase in the pickup ion mediated solar wind temperature leading to the sound speed increase beyond the ionization cavity (Zank & Pauls 1997; Rice & Zank 1999; Rice et al. 2000).

This work is funded by the Science and Engineering Research Board (SERB, grant No. SB/S2/RJN-080/2018), a statutory body of the Department of Science and Technology

(DST), Government of India through a Ramanujan Fellowship. The high-resolution Voyager spacecraft observations analyzed in this work are obtained from NASA's COHWeb (<https://omniweb.gsfc.nasa.gov/coho/>). The daily  $F_{10.7}$  solar flux are obtained from the Laboratory for Atmospheric and Space Physics (LASP) Interactive Solar Irradiance Data Center (<https://lasp.colorado.edu/lisird/>). I would like to thank the reviewer and editor Dr. Gary Zank for extremely valuable suggestions that substantially improved the manuscript.

### ORCID iDs

Rajkumar Hajra  <https://orcid.org/0000-0003-0447-1531>

### References

- Abraham-Shrauner, B., & Yun, S. H. 1976, *JGRA*, **81**, 2097
- Balogh, A., Bothmer, V., Crooker, N. U., et al. 1999, *SSRv*, **89**, 141
- Balogh, A., Forsyth, R. J., Ahuja, A., et al. 1993, *AdSpR*, **13**, 15
- Bavassano-Cattaneo, M. B., Tsurutani, B. T., Smith, E. J., & Lin, R. P. 1986, *JGRA*, **91**, 11929
- Behannon, K. W. 1978, *RvGeo*, **16**, 125
- Burlaga, L., Sittler, E., Mariani, F., & Schwenn, R. 1981, *JGRA*, **86**, 6673
- Burlaga, L. F., Mish, W. H., & Whang, Y. C. 1990, *JGRA*, **95**, 4247
- Burlaga, L. F., Ness, N. F., Wang, Y.-M., & Sheeley, N. R., Jr. 2002, *JGRA*, **107**, 20
- Cane, H. V. 1985, *JGRA*, **90**, 191
- Echer, E. 2019a, *GeoRL*, **46**, 5681
- Echer, E. 2019b, *P&SS*, **165**, 210
- Echer, E., Gonzalez, W. D., Vieira, L. E. A., et al. 2003, *BrJPh*, **33**, 115
- Echer, E., Tsurutani, B. T., & Guarnieri, F. L. 2010, *AdSpR*, **45**, 798
- Gazis, P. R. 1996, *RvGeo*, **34**, 379
- González-Esparza, J. A., Balogh, A., Forsyth, R. J., et al. 1996, *JGRA*, **101**, 17057
- González-Esparza, J. A., Neugebauer, M., Smith, E. J., & Phillips, J. L. 1998, *JGRA*, **103**, 4767
- Gopalswamy, N., Nunes, S., Yashiro, S., & Howard, R. A. 2004, *AdSpR*, **34**, 391
- Gosling, J. T., Bame, S. J., McComas, D. J., et al. 1994, *GeoRL*, **21**, 237
- Gosling, J. T., Bame, S. J., McComas, D. J., & Phillips, J. L. 1990, *GeoRL*, **17**, 901
- Gosling, J. T., Bame, S. J., Smith, E. J., & Burton, M. E. 1988, *JGRA*, **93**, 8741
- Hajra, R. 2021, *SoPh*, **296**, 33
- Hajra, R., Echer, E., Tsurutani, B. T., & Gonzalez, W. D. 2013, *JGRA*, **118**, 5626
- Hajra, R., Henri, P., Myllys, M., et al. 2018, *MNRAS*, **480**, 4544
- Hajra, R., & Tsurutani, B. T. 2018a, *ApJ*, **858**, 123
- Hajra, R., & Tsurutani, B. T. 2018b, in *Extreme Events in Geospace*, ed. N. Buzulukova (Amsterdam: Elsevier), 373
- Hajra, R., Tsurutani, B. T., Echer, E., & Gonzalez, W. D. 2014, *GeoRL*, **41**, 1876
- Hajra, R., Tsurutani, B. T., Echer, E., Gonzalez, W. D., & Gjerloev, J. W. 2016, *JGRA*, **121**, 7805
- Hajra, R., Tsurutani, B. T., & Lakhina, G. S. 2020, *ApJ*, **899**, 3
- Hoang, S., Lacombe, C., Mangeney, A., et al. 1995, *AdSpR*, **15**, 371
- Holzer, T. E. 1972, *JGRA*, **77**, 5407
- Hugoniot, H. 1887, *J. Ec. Polytech.*, **57**, 3
- Hugoniot, H. 1889, *J. Ec. Polytech.*, **58**, 1
- Hundhausen, A. J., & Gosling, J. T. 1976, *JGRA*, **81**, 1436
- Jian, L., Russell, C. T., Luhmann, J. G., & Skoug, R. M. 2006, *SoPh*, **239**, 337
- Kennel, C. F., Edmiston, J. P., & Hada, T. 1985, *A Quarter Century of Collisionless Shock Research* (Washington, DC: AGU), 1
- Kilpua, E. K. J., Lumme, E., Andreeva, K., Isavnin, A., & Koskinen, H. E. J. 2015, *JGRA*, **120**, 4112
- Klein, L. W., & Burlaga, L. F. 1982, *JGRA*, **87**, 613
- Landau, L. D., & Lifshitz, E. M. 1960, *Electrodynamics of Continuous Media* (2nd ed.; New York: Pergamon)
- Luhmann, J. G. 1995, *AdSpR*, **15**, 355
- Neugebauer, M. 2013, *SSRv*, **176**, 125
- Obridko, V. N., Ivanov, E. V., Özgüç, A., Kilcik, A., & Yurchyshyn, V. B. 2012, *SoPh*, **281**, 779
- Parker, E. N. 1965, *SSRv*, **4**, 666
- Press, W. H., Teukolsky, S. A., Vetterling, W. T., & Flannery, B. P. 1992, *Numerical Recipes: The Art of Scientific Computing* (2nd ed.; New York: Cambridge Univ. Press)
- Rankine, W. J. M. 1870, *RSPT*, **160**, 277
- Reiff, P. H. 1990, *JGG*, **42**, 1145
- Rice, W. K. M., & Zank, G. P. 1999, *JGRA*, **104**, 12563
- Rice, W. K. M., Zank, G. P., Richardson, J. D., & Decker, R. B. 2000, *GeoRL*, **27**, 509
- Richardson, I. G. 2014, *SoPh*, **289**, 3843
- Richardson, J. D., & Wang, C. 2005, in *AIP Conf. Proc. 781, The Physics of Collisionless Shocks* (New York: AIP), 278
- Sheeley, N. R., Harvey, J. W., & Feldman, W. C. 1976, *SoPh*, **49**, 271
- Sheeley, N. R., Jr., Howard, R. A., Koomen, M. J., et al. 1985, *JGRA*, **90**, 163
- Siscoe, G. L. 1972, *JGRA*, **77**, 27
- Smith, E. J. 1985, *Interplanetary Shock Phenomena Beyond 1 au* (Washington, DC: AGU), 69
- Smith, E. J., & Wolfe, J. H. 1976, *GeoRL*, **3**, 137
- Sonett, C. P., & Colburn, D. S. 1965, *P&SS*, **13**, 675
- Student 1908, *Biometrika*, **6**, 1
- Tsurutani, B. T., & Gonzalez, W. D. 1997, *The Interplanetary Causes of Magnetic Storms: A Review* (Washington, DC: AGU), 77
- Tsurutani, B. T., Gonzalez, W. D., Tang, F., Akasofu, S. I., & Smith, E. J. 1988, *JGRA*, **93**, 8519
- Tsurutani, B. T., Ho, C. M., Arballo, J. K., Goldstein, B. E., & Balogh, A. 1995, *GeoRL*, **22**, 3397
- Tsurutani, B. T., Lakhina, G. S., & Hajra, R. 2020, *NPGeo*, **27**, 75
- Tsurutani, B. T., Lakhina, G. S., Verkhoglyadova, O. P., et al. 2011, *JASTP*, **73**, 5
- Tsurutani, B. T., & Lin, R. P. 1985, *JGRA*, **90**, 1
- Wang, C., Richardson, J. D., & Burlaga, L. 2001, *SoPh*, **204**, 413
- Zank, G. P. 1999, *SSRv*, **89**, 413
- Zank, G. P., Adhikari, L., Zhao, L.-L., et al. 2018, *ApJ*, **869**, 23
- Zank, G. P., & Pauls, H. L. 1997, *JGRA*, **102**, 7037